Appl. Phys. A (2015) 118:249–260
DOI 10.1007/s00339-014-8669-8

Applied Physics A
Materials Science & Processing

Influence of Li^+ and Dy^{3+} on structural and thermoluminescence studies of sodium sulfate

Y. S. Vidya · B. N. Lakshminarasappa

Received: 15 December 2013 / Accepted: 2 August 2014 / Published online: 19 August 2014

Abstract Na_2SO_4, Na_2SO_4: Dy^{3+}, $LiNaSO_4$ and $LiNaSO_4$: Dy^{3+} nanoparticles successfully synthesized by slow evaporation technique followed by calcination at 400 °C. The resultant products were characterized by powder X-ray diffraction, scanning electron microscopy, transmission electron microscopy, Fourier transform infrared and UV–Vis spectroscopy. The average crystallite size was calculated using Debye–Scherrer's formula and Williamson–Hall's (W–H) plots. The optical energy band gap (E_g) was estimated from Wood and Tauc's relation, which varies from 3.70 to 4.45 eV. The variation in band gap values attributed to large degree of structural defects. Thermoluminescence studies were investigated using γ-irradiation in the dose range 0.5–5 kGy at a heating rate of 5 K s^{-1}. The samples Na_2SO_4 and $LiNaSO_4$ showed a well-resolved glow peak at ~180 and ~170 °C, respectively. The prominent glow peak at ~175 °C along with shouldered peak at ~60 °C was observed for Na_2SO_4: Dy^{3+}. $LiNaSO_4$: Dy^{3+} showed prominent glow peak at ~100 °C and a small shoulder peak at ~180 °C. The addition of isovalent (Li^+) quenches the TL intensity, whereas the hypervalent (Dy^{3+}) increases the intensity of Na_2SO_4. The variations of TL intensity for all the phosphors follow linear behavior up to 5 kGy and were useful in radiation dosimetry. The kinetic parameters (*E, b* and *s*) were estimated from the glow peak shape method.

Electronic supplementary material The online version of this article (doi:10.1007/s00339-014-8669-8) contains supplementary material, which is available to authorized users.

Y. S. Vidya · B. N. Lakshminarasappa (✉)
Department of Physics, Jnana Bharathi Campus, Bangalore University, Bangalore 560 056, India
e-mail: bnlnarasappa@rediffmail.com

1 Introduction

Rare earth (RE) ions activated phosphors have attracted much attention of scientists due to their unique electronic, optical and chemical properties resulted from the 4f shell of the ion; also, the progress in the development of the phosphors was directly related to the understanding of the physical processes of energy absorption and relaxation [1–3]. Thus, the f–f transition absorption and emission of the trivalent lanthanide ions in crystalline hosts were receiving more attention as optical materials emitting in the visible and near IR regions [4, 5]. RE ion-doped sulfates have been widely used as novel luminescent materials in cathode ray tubes and plasma display panels due to their high luminescence efficiency [6]. In the family of sulfate phosphors, calcium sulfate was one of the most sensitive TL phosphor and it was in fact the first one used to measure ionizing radiation in 1895 [7–10]. Sodium sulfate was yet another material that has been quite popular among the researchers in this field. Sodium sulfate (thenardite), though very simple in chemical composition, has been the subject of various applications. It was used for the production of glasses and paints and for thermal energy storage techniques [11, 12]. In order to develop new dosimetric materials and to obtain a better understanding of the physical mechanism of radiation effects, Na_2SO_4 was doped and codoped with activators.

At room temperature (RT), phase V (thenardite) of Na_2SO_4 was reported to be stable while phase III was metastable. Phases I and II were high-temperature polymorphs; however, phase II was reported to have a narrow stability zone. Phase IV was considered to be metastable, and its phase relation and structure have yet to be well established [13–16]. Mixed sulfates such as $K_2Ca_2(SO_4)_3$

and $LiNaSO_4$ have been of much interest to researchers [17–20]. Till to the date, only few works were reported on the luminescence studies of doped/codoped sodium sulfate [21–23]. Correcher et al. observed the spectra of infrared-stimulated luminescence (IRSL), radioluminescence (RL) and TL studies in the range of 200–800 nm on phase transitions of Na_2SO_4 [24]. Previous TL studies on $LiNaSO_4$: Eu^{3+} revealed that the phosphor was more sensitive than the commercially available phosphors like TLD 100 and $CaSO_4$: Dy [25, 26].

As far as the synthesis method was concerned, alkali sulfate samples were generally synthesized by solid-state and melt method [27]. Among various techniques, slow evaporation technique, even though the rate of crystallization is slow, occupies a prominent place owing to its versatility and simplicity. Slow evaporation technique, though it takes long duration, was well suited to those materials which suffer from decomposition in the melt or in the solid at high temperatures and which undergo structural transformations while cooling from melting point. The solid-state/melt method has some short comings, such as energy consuming, inhomogeneous mixing and product with irregularly shaped and aggregated particles [28]. The principal advantage of slow evaporation method is that since crystal growth occurs at room temperature, the structural imperfections are relatively low and crystals grow with well-defined faces. The luminescent properties of the phosphors were strongly affected by the preparation method, which was the dominant factor for improving particle size and morphology [29, 30]. Growth of crystals from solution at RT has many advantages over other growth methods though the rate of crystallization was slow. Since the growth was carried out at RT, the structural imperfections in solution grown crystals were relatively low. It was well suited to those materials which suffer from decomposition in the melt or in the solid at high temperature and which undergo structural/phase transformations while cooling from the melting point. Number of studies reported on the solubility and crystal growth mechanism by slow evaporation technique [31, 32].

The present study reports slow evaporation technique that produces homogeneous, crystalline and fine powders of Na_2SO_4, Na_2SO_4: Dy^{3+}, $LiNaSO_4$ and $LiNaSO_4$: Dy^{3+} samples. The synthesized samples were well characterized using powder X-ray diffractometer (PXRD), scanning electron microscopy (SEM), transmission electron microscopy (TEM), Fourier transform infrared spectroscopy (FTIR) and UV–Vis absorption spectra. Thermoluminescence (TL) studies were carried out by irradiating the samples with γ-irradiation in the dose range 0.5–5 kGy to explore the possibility of the material as TL dosimeter.

2 Experimental

2.1 Materials preparation

Saturated solution of Na_2SO_4 was obtained by dissolving 6 g of sodium sulfate (S–d fine) in 20 ml of deionized water at room temperature (30 °C). To prepare $LiNaSO_4$, stoichiometrically calculated Li_2SO_4 (0.5 mol %) procured from S–d fine was weighed and dissolved in 10 ml of double-distilled deionized water and added to Na_2SO_4 solution. For Na_2SO_4: Dy^{3+}, stoichiometrically calculated amount Dy_2O_3 (procured from E. Merck) was weighed and dissolved in 10 ml of concentrated H_2SO_4 and added to Na_2SO_4 solution to get Dy/Na mole ratio 0.5 %. To prepare $LiNaSO_4$: Dy^{3+}, stoichiometrically calculated Dy_2O_3 was weighed and dissolved in 10 ml of concentrated H_2SO_4 and added to $LiNaSO_4$ solution to get Dy/Na mole ratio 0.2, 0.5 and 1 %.

All the above solutions taken in beakers are allowed to undergo slow evaporation at RT in an open air atmosphere for a period of 10–15 days. The resultant compound was crushed and calcined at 400 °C for 4 h in muffle furnace. After cooling to RT, it was further crushed to fine powder and used to characterize the samples. For TL measurements, the obtained fine powder was pressed into pellets of 1 mm thickness with 5 mm in diameter at an applied pressure of 80 kg cm^{-2} using a homemade pelletizer.

2.2 Material characteristics

The phase purity and the crystallinity of the samples were examined by PXRD (Philips PW/1050/70/76 X- ray diffractometer) using CuK_α (1.541 Å) radiation with a nickel filter at a scan rate of 2 degree min^{-1}. The surface morphology of the products was examined by SEM (Quanta—200 FEI SEM) equipped with EDS operating at 10–20 kV, and TEM analysis was performed on a Philips CM 200 microscope operating between 20 and 200 kV with 2.4 Å resolutions. FT-IR studies of the samples were performed on a Perkin–Elmer FTIR spectrometer (Spectrum 1000) with KBr pellets. The UV–Vis absorption spectra of the samples were recorded using UV–Visible Shimadzu double-beam spectrophotometer.

TL measurements were carried out using homemade TL setup in the temperature range 25–300 °C at a heating rate of 5 K s^{-1}. TL glow curve recorder consists of the following: (i) TL detection head where the sample was heated on a Kanthal strip heater; (ii) EHT—high-voltage DC power supply provides the high voltage (−850 V) needed for photomultiplier tube (PMT) operation with a maximum current rating of 1 mA. It supplies a maximum of 1,250 V DC, through a single pin Amphenol connector, mounted on the rear panel of the instrument; (iii) Model 1,100

Electrometer amplifier; and (iv) data acquisition system. The sample was heated on a Kanthal strip heater where a Chromel–Alumel thermocouple was spot-welded to the heater strip for sensing the sample temperature. All the TL glow curve measurements were made at RT after γ-irradiation where the samples were exposed to source ^{60}Co for a dose range 0.5–5 kGy. In the present study, quartz plate is used as IR filters.

3 Results and discussion

3.1 PXRD analysis

The PXRD patterns of calcined Na_2SO_4, Na_2SO_4: Dy^{3+} (0.5 %), $LiNaSO_4$ (0.5 %) and $LiNaSO_4$: Dy^{3+} (0.2, 0.5 and 1.0 mol%) samples are shown in Fig. 1. The diffraction patterns of Na_2SO_4 were in good agreement with ICDD card 37–1,465 (Phase V, Thenardite). $LiNaSO_4$ exhibited pristine phase while Na_2SO_4: Dy^{3+} and $LiNaSO_4$: Dy^{3+} resulted in the phase transformation from stable thenardite to metastable mirabilite phase (phase III) [33]. The thenardite to mirabilite phase transformation was generally considered as a nucleation growth process during which the mirabilite nuclei were formed within the thenardite phase. The mirabilite content increases with increase in the concentration of Dy^{3+} ion. Further, the particle size was calculated by Scherrer's method [34].

$$D = \frac{0.9\ \lambda}{\beta\ \cos\ \theta} \tag{1}$$

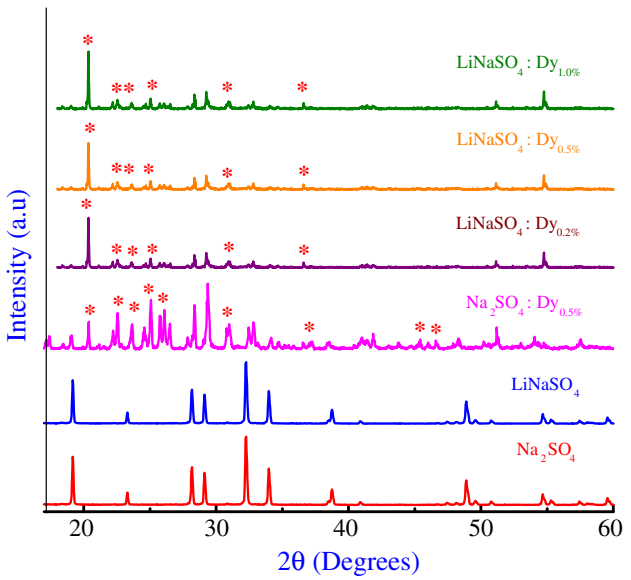

Fig. 1 PXRD patterns of pure Na_2SO_4, $LiNaSO_4$, Na_2SO_4: Dy^{3+} and $LiNaSO_4$: Dy^{3+} at RT (the peaks with *asterisks* correspond to mirabilite phase)

where '*D*'is the average grain size of the crystallites, 'λ' the incident wavelength, 'θ' the Bragg angle and 'β': the diffracted full width at half maximum (in radians) caused by the crystallites. The average grain size of Na_2SO_4, Na_2SO_4: Dy^{3+}, $LiNaSO_4$ and $LiNaSO_4$: Dy^{3+} samples was estimated to be in the range 55, 38, 40 and 30 nm, respectively. The crystallite size, full-width half-maxima (FWHM) values are tabulated in Table 1S.

Williamson and Hall (W–H) have suggested a method [35] combining the domain size and lattice micro-strain effects on line broadening, when both were operative. The W–H approach considers the case when the domain effect and lattice deformation were both simultaneously operative and their combined effects give the final line broadening FWHM (β), which was the sum of grain size and lattice distortion. This relation assumes a negligibly small instrumental contribution compared with the sample-dependent broadening. W–H equation may be expressed in the form

$$\beta\ \cos\theta\ =\ \varepsilon(4\ \sin\theta) + \frac{\lambda}{D} \tag{2}$$

where β (FWHM in radians) was measured for different XRD lines corresponding to different planes, 'ε' the strain developed and *D* the grain size. The equation represents a straight line between 4 sinθ (*X*-axis) and β cosθ (*Y*-axis). The slope of the line gives the strain (ε), and intercept (λ/*D*) of this line on the *Y*-axis gives grain size (*D*). Figure 2 shows the W–H plots of Na_2SO_4, Na_2SO_4: Dy^{3+}, $LiNaSO_4$ and $LiNaSO_4$: Dy^{3+} samples.

The grain size determined from W–H plots (Na_2SO_4—58 nm, Na_2SO_4: Dy^{3+}—39 nm, $LiNaSO_4$—42 nm and $LiNaSO_4$: Dy^{3+}—32 nm) was slightly higher than those

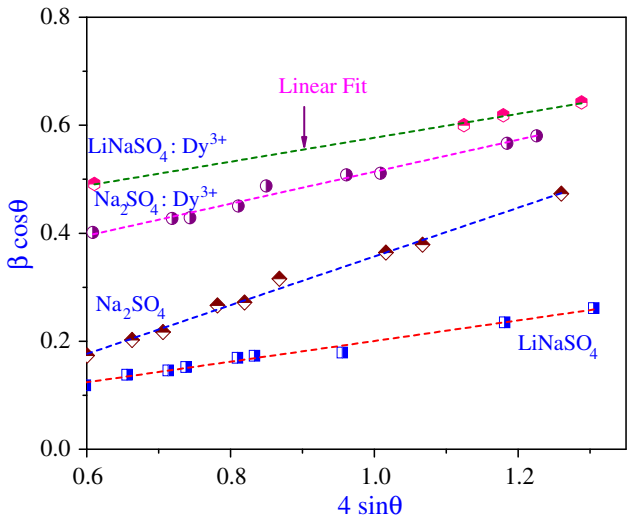

Fig. 2 Williamson–Hall's plots of Na_2SO_4, Na_2SO_4: Dy^{3+}, $LiNaSO_4$ and $LiNaSO_4$: Dy^{3+} nanoparticles

calculated using Scherrer's formula. The small variation in the values was due to strain component was assumed to be zero, and observed broadening of diffraction peak was considered as a result of reducing grain size in Scherrer's formula. Further, it was observed that the strain for Na_2SO_4, Na_2SO_4: Dy^{3+}, $LiNaSO_4$ and $LiNaSO_4$: Dy^{3+} was found to be 1.134×10^{-3}, 0.983×10^{-3}, 1.02×10^{-3} and 0.738×10^{-3}, respectively.

Lattice parameters (a, b and c) for orthorhombic Na_2SO_4, Na_2SO_4: Dy^{3+}, $LiNaSO_4$ and $LiNaSO_4$: Dy^{3+} were calculated by the following relation:

$$d^2 = \left(\frac{h^2}{a^2} + \frac{k^2}{b^2} + \frac{l^2}{c^2}\right)^{-1} \quad (3)$$

a, b and c refer to the lattice parameters, and h, k and l were the miller indexes while d was the crystalline face space. The calculated lattice parameters were comparable as reported in the literature [36], and they are tabulated in Table 2S. From the table, it was observed that in $LiNaSO_4$: Dy^{3+}, the value of c dimension changes while a and b remain almost constant for the range of dopant concentration (0.2, 0.5 and 1 mol%). Thus, with increase in dopant concentration, the crystal growth proceeds along c axis. It was worth noting that diffraction peaks corresponding to Dy^{3+} or its sulfates were not detected in the PXRD patterns due to the complete solubility of Dy^{3+} ions in the Na_2SO_4 matrix. Since no characteristic peaks corresponding to Dy^{3+} species were present, it can be concluded that the metal ion loading was below the dispersion capacity.

3.2 SEM and TEM analyses

SEM and TEM analyses were carried out to study the morphology and particle size of the crystallites of the nanoparticles. Figure 3a, c, e, g shows the SEM images of Na_2SO_4, Na_2SO_4: Dy^{3+}, $LiNaSO_4$ and $LiNaSO_4$: Dy^{3+} samples. The surface morphology showed the generalized hexagonal habit of grains corresponds to twinned orthorhombic prisms and pyramids without any agglomeration. $LiNaSO_4$ was slightly agglomerated compared with all other samples. The element and atomic composition of all the samples obtained from EDX analysis are listed in Fig. 3b, d, f, h. The EDX analysis reveals that the added dopants were well incorporated in Na^+ lattice sites. The TEM images of Na_2SO_4, Na_2SO_4: Dy^{3+}, $LiNaSO_4$ and $LiNaSO_4$: Dy^{3+} confirm the orthogonal prisms and pyramidal shape with no amorphous constituents and weekly aggregated (Fig. $4A_1$–A_4, respectively). The average crystallite sizes obtained from TEM analysis were in good agreement with the value obtained from Scherrer's formula. SAED patterns of these samples were neither regular diffraction spots nor whole diffraction rings, indicating that the number of polycrystalline grains in the selected area was finite (Fig. $4B_1$–B_4). The interplanar distance d values and hkl values obtained for different spots in SAED pattern are tabulated in Table 3S.

Fig. 3 SEM images and their corresponding EDX spectra of Na_2SO_4 (**a**, **b**), $LiNaSO_4$ (**c**, **d**), Na_2SO_4: Dy^{3+} (**e**, **f**), $LiNaSO_4$: Dy^{3+} (**g**, **h**) nanoparticles

3.3 FTIR analysis

Figure 5 gives the FTIR spectra of (a) Na_2SO_4, (b) Na_2SO_4: Dy^{3+} (0.5 %), (c) $LiNa_2SO_4$ (0.5 %) and (d) $LiNaSO_4$: Dy^{3+} (0.5 %) samples in the range 400–4,000 cm^{-1}, respectively. Table 4S shows the frequencies of all the observed absorption bands. In the obtained spectra, it was possible to distinguish clearly the ranges corresponding to the vibrations of the SO_4^{2-} group and the Na–O vibrations [37]. The most intense bands were due to stretching and bending of S–O bonds was situated at 1,100 and 600 cm^{-1}, respectively.

3.4 UV–Vis absorption and Optical band gap energy

Inset of Fig. 6 shows the UV–Vis absorption spectra of Na_2SO_4, Na_2SO_4: Dy^{3+}, $LiNaSO_4$ and $LiNaSO_4$: Dy^{3+} samples with optical band gap energy. The optical absorption spectrum of Na_2SO_4 has prominent absorption peaks at ~219, ~261, ~327, 554 and 580 nm which correspond to O–H group of mirabilite phase [38]. On doping with Li^+/Dy^{3+}, the curve becomes smooth and slight red shift was observed. In $LiNaSO_4$, since the ionic radii of Li^+ are small compared with Na^+, almost same absorption peaks were observed, whereas in the case of Na_2SO_4: Dy^{3+} and $LiNaSO_4$: Dy^{3+}, a broad absorption curve was observed at ~265 and ~267 nm which was attributed to intraconfigurational *4f–4f* transitions of Dy^{3+} from the ground state. The remaining weak absorptions were expected to arise from transitions involving extrinsic states such as surface traps or defect states or impurities [39]. Smaller sized particles were found to have high surface to volume ratio. This results in increase in the number of defects distribution on the surface of nanomaterials. Thus, if the particle size was small, nanomaterials exhibit strong and broad absorption bands [40]. In Na_2SO_4, Na_2SO_4: Dy^{3+}, $LiNaSO_4$ and $LiNaSO_4$: Dy^{3+}, the particle sizes were in nanometers which results in high surface to volume ratio; as a result, there was an increase in defects distribution on the surface of the nanomaterials.

For the estimation of band gap in nanomaterials, the absorbance spectra of Na_2SO_4, Na_2SO_4: Dy^{3+}, $LiNaSO_4$

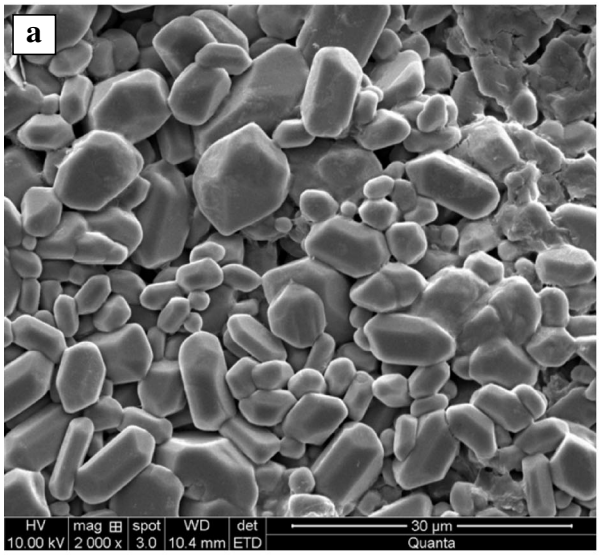

b

Element	Weight (%)	Atom %
O (K)	21.84	36.90
Na (K)	0.075	1.520
S (K)	77.41	61.58

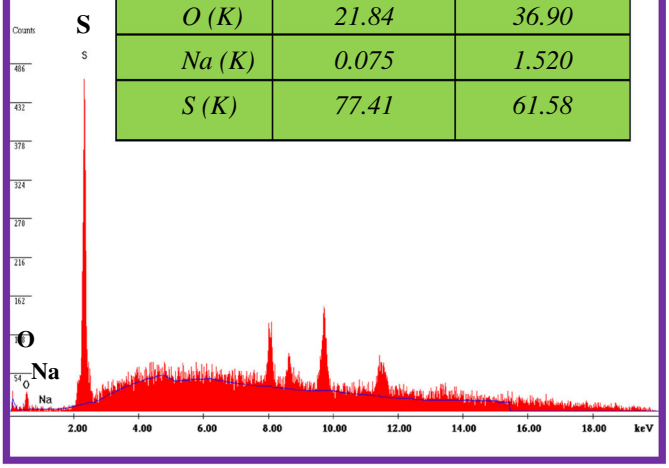

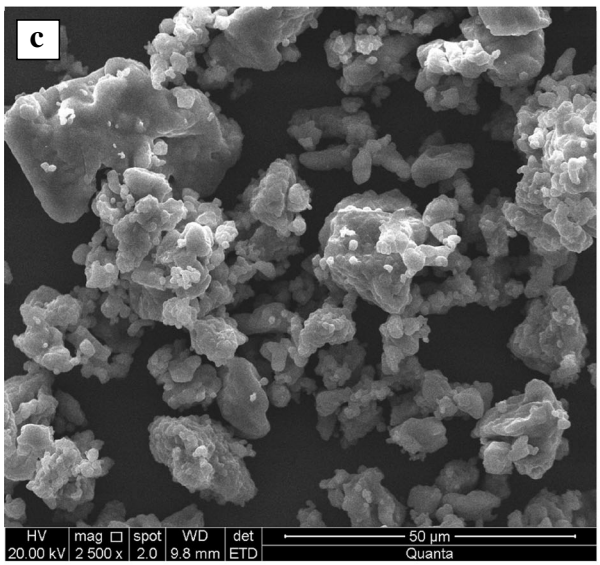

d

Element	Weight (%)	Atom %
O (K)	21.62	36.90
Na (K)	0.072	1.492
Li (K)	1.078	0.028
S (K)	78.23	61.58

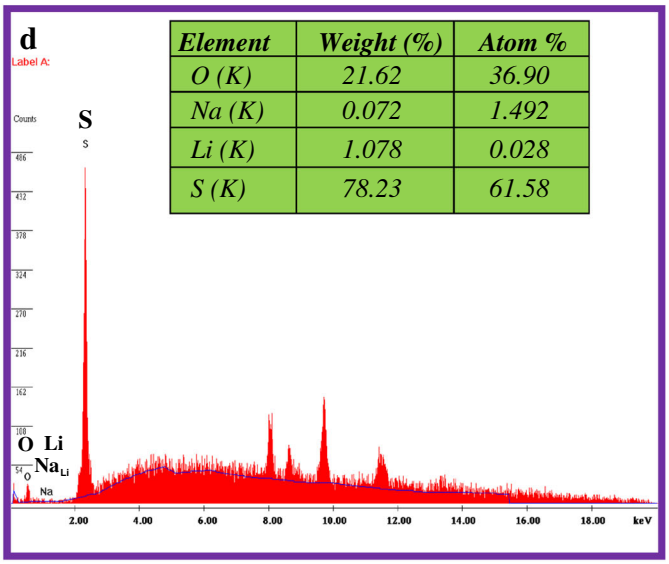

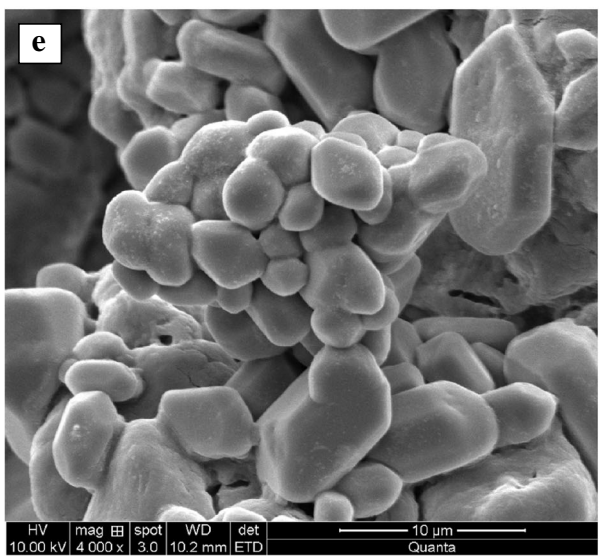

f

Element	Weight (%)	Atom %
O (K)	12.41	22.90
Na (K)	0.351	0.580
Dy (L)	32.32	67.08
S (K)	54.82	9.440

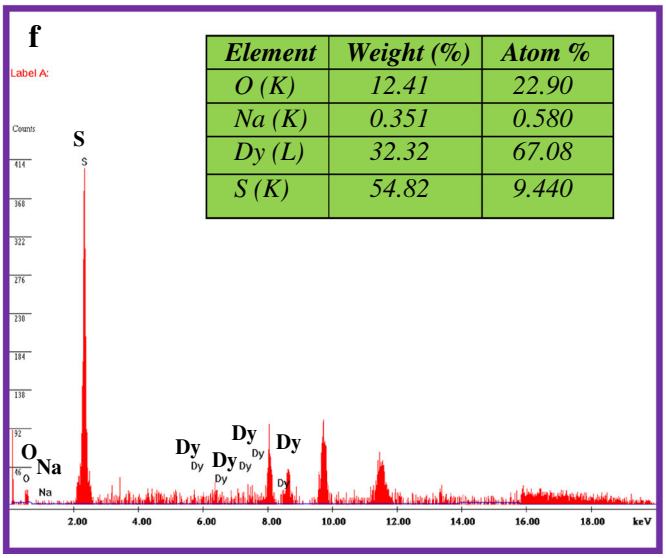

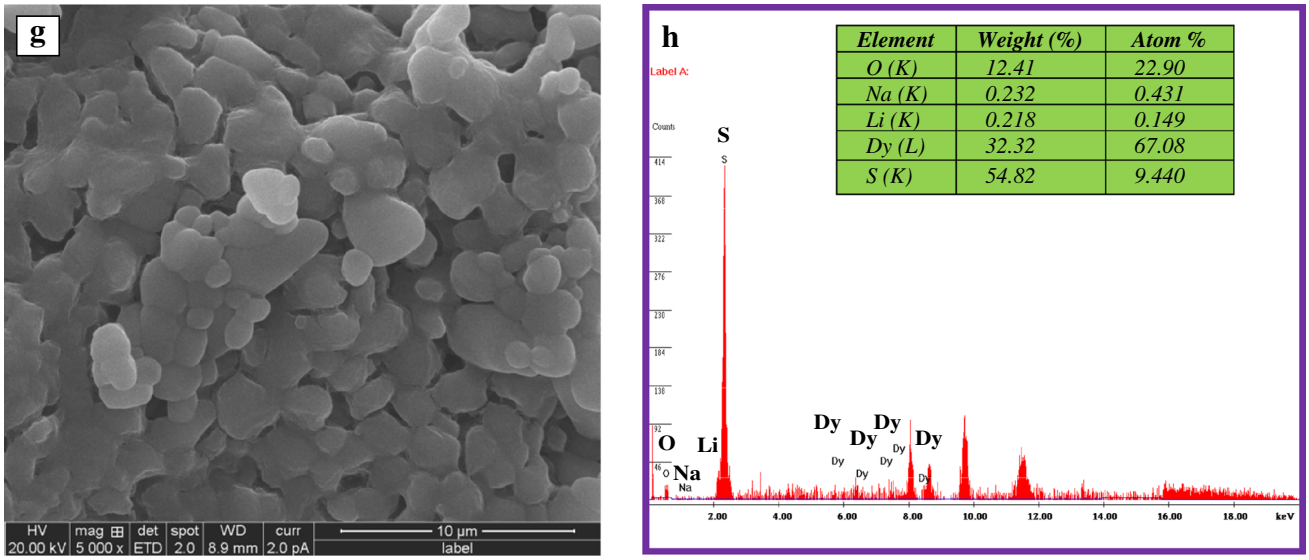

Element	Weight (%)	Atom %
O (K)	12.41	22.90
Na (K)	0.232	0.431
Li (K)	0.218	0.149
Dy (L)	32.32	67.08
S (K)	54.82	9.440

Fig. 3 continued

and $LiNaSO_4$: Dy^{3+} nanoparticles in transmission mode were recorded by distributing the particles uniformly in liquid paraffin, in the wavelength range of 200–800 nm. For a direct band gap material, the absorption coefficient near the band edge was given by Tauc's relation [41].

$$\alpha = \frac{A}{h\nu}(h\nu - E_g)^{1/2} \tag{4}$$

where a is the absorption co-efficient, $h\nu$ the photon energy, E_g the energy band gap and A the constant depending on the type of transition. Equation (4) can be rearranged and written in the form

$$(\alpha h\nu)^2 = A^2(h\nu - E_g) \tag{5}$$

From Eq. (5), it was clear when $\alpha h\nu = 0$, $E_g = h\nu$.

The energy gap was determined by plotting $(\alpha h\nu)^2$ versus $h\nu$ and finding the intercept on the $h\nu$ axis by extrapolating the plot to $(\alpha h\nu)^2 = 0$ as shown in Fig. 6.

Band gap energy (E_g) observed for Na_2SO_4, $LiNaSO_4$, Na_2SO_4: $Dy^{3+}$and $LiNaSO_4$: Dy^{3+} was found to be 4.45, 4.23, 4.02 and 3.70, respectively. A reduction in E_g for doped/codoped samples would arise neither from a quantum size effect nor from crystal structure variation but rather from surface traps states or point defects. A plausible explanation for the variations observed on the E_g values can be related to the degree of structural order–disorder into the lattice, which is able to change the intermediary energy-level distribution within the band gap. The E_g values mainly depend on the preparation methods and the experimental conditions. In particular, these key factors can favor on inhibit the formation of structural defects which are able to control the degree of structural order–disorder of the material and, consequently, the number of intermediary energy levels within the band gap. It was observed that the absorption measurements were extremely sensitive to the changes in the lattice or variations on the structural order–disorder degree [42].

3.5 Thermoluminescence (TL) studies

TL glow curve under a specific radiation type was characteristic of the exposed material. The traps and glow curve structure were also dependent upon the morphology and particle size. It is important to notice that using the proper dopant concentration, it was possible to maximize the TL efficiency and improve sensitivity and dose linearity for specific irradiation type [43–45]. In the present study, the TL measurements of γ-irradiated Na_2SO_4, Na_2SO_4: Dy^{3+}, $LiNaSO_4$, $LiNaSO_4$: Dy^{3+} nanophosphor materials were carried out at RT at a heating rate of 5 Ks^{-1}.

TL property of host sample was investigated at different γ-ray dose levels (Fig. 7a). The pure orthorhombic phosphor has a prominent glow peak at ~180 °C with a small shoulder with peak at ~104 °C which indicates the presence of two kind of trapping sites generated during γ-irradiation. The shallow trapping center leads to a shoulder peaks (~104° C), and the deeper center gives rise to prominent glow peak at high temperature (~180° C). The intensity of these glow peaks increases with irradiation and shifts toward higher-temperature region. The indication of two TL glow peaks reveals that there must be at least two

Fig. 4 TEM images and selected-area electron diffractions of ▶ Na_2SO_4 (**A**$_1$, **B**$_1$), Na_2SO_4:Dy^{3+} (**A**$_2$, **B**$_2$), $LiNaSO_4$ (**A**$_3$, **B**$_3$) and $LiNaSO_4$: Dy^{3+} (**A**$_4$, **B**$_4$) nanoparticles

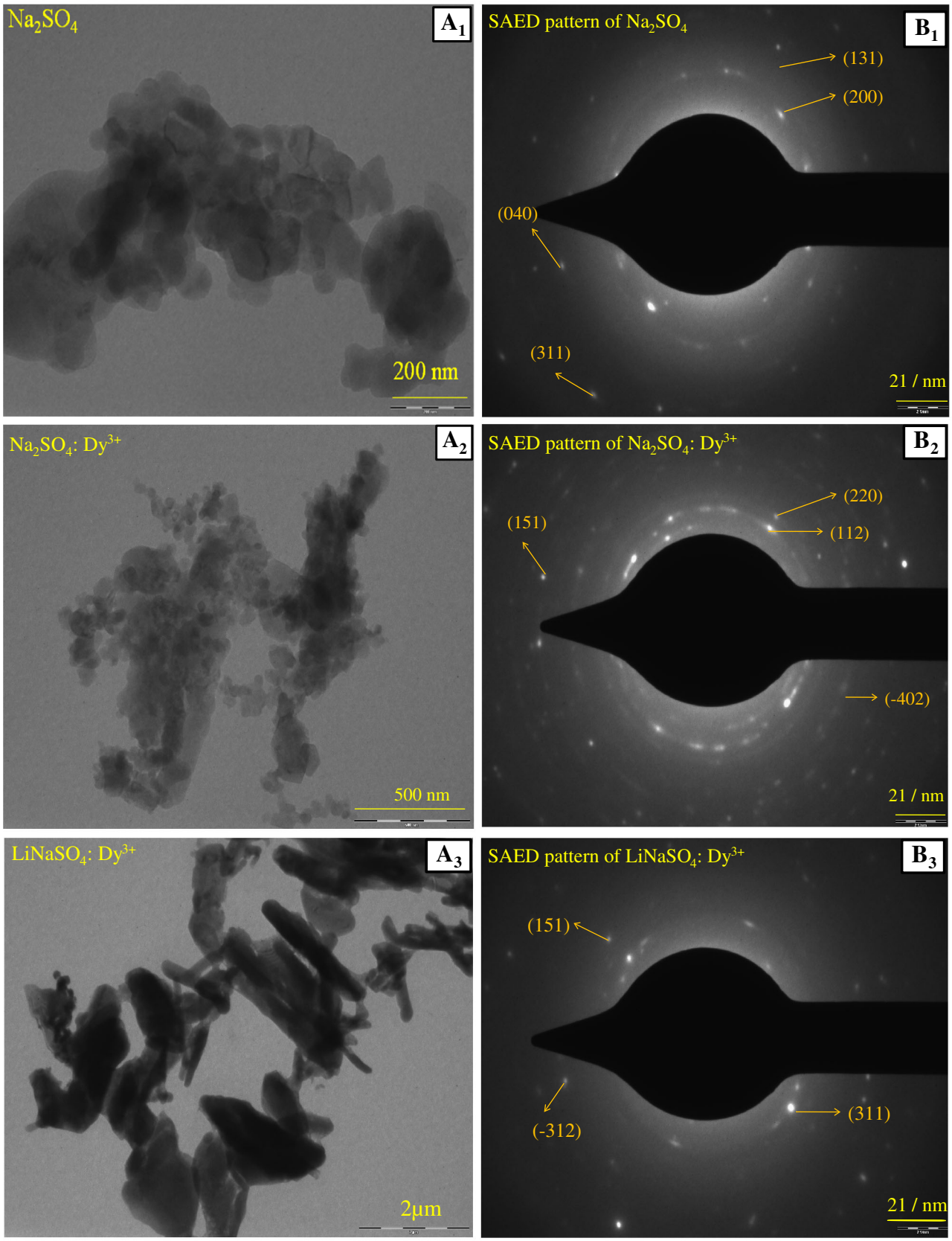
Na_2SO_4
A1
200 nm
SAED pattern of Na_2SO_4
B1
(131)
(200)
(040)
(311)
21 / nm
Na_2SO_4: Dy^{3+}
A2
500 nm
SAED pattern of Na_2SO_4: Dy^{3+}
B2
(220)
(151)
(112)
(-402)
21 / nm
$LiNaSO_4$: Dy^{3+}
A3
2μm
SAED pattern of $LiNaSO_4$: Dy^{3+}
B3
(151)
(-312)
(311)
21 / nm

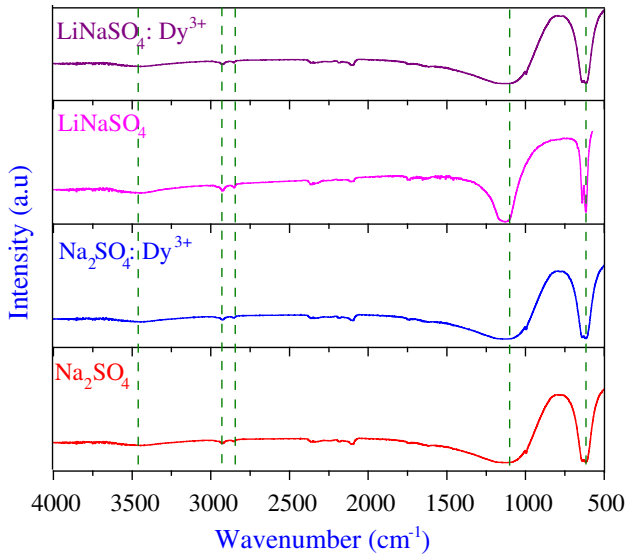

Fig. 5 FTIR spectra of Na_2SO_4, Na_2SO_4: Dy^{3+}, $LiNaSO_4$ and $LiNaSO_4$: Dy^{3+} at RT

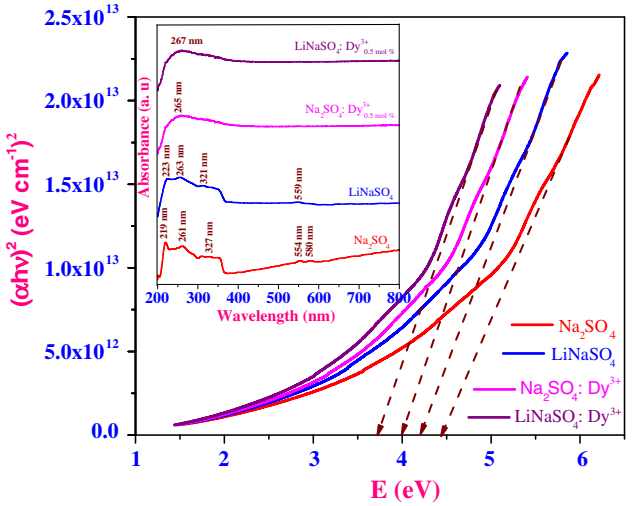

Fig. 6 UV–Vis absorption spectra and band energy gap of Na_2SO_4, Na_2SO_4: Dy^{3+}, $LiNaSO_4$ and $LiNaSO_4$: Dy^{3+} nanoparticles

defect centers among them one might be related to hole traps and other one may be related to electron trap (s).

Figure 8a shows the TL glow curves recorded for $LiNaSO_4$ irradiated with γ-rays in the range 0.5–5 kGy. The $LiNaSO_4$ phosphor has a single well-resolved glow peak at 155° C with a small shoulder at 120 and 187 °C. The indication of three TL glow peaks reveals that there must be at least three defect centers among them two might be related to hole traps and other one may be related to electron trap (s). The presence of lithium ion caused a reduction in the TL intensity with slightly shifting the glow peak positions toward higher temperature. This process

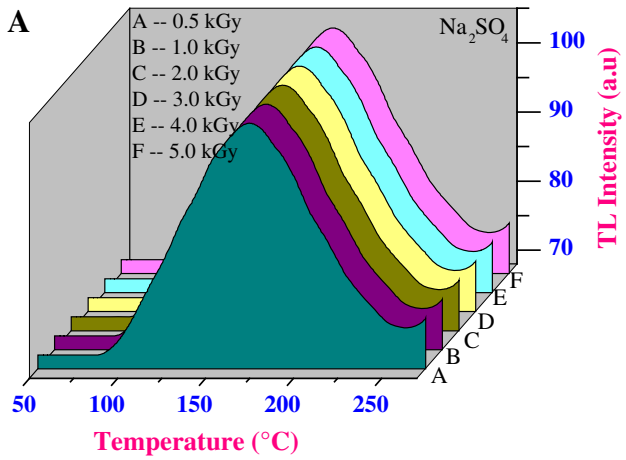

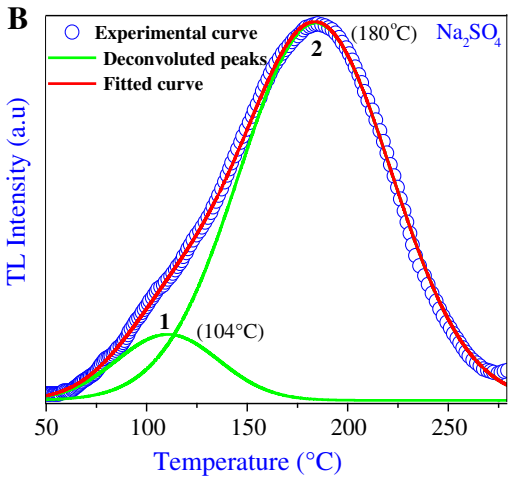

Fig. 7 **a** TL glow curves of γ-irradiated Na_2SO_4 nanophosphor (0.5–5 kGy), **b** deconvoluted TL glow curve of 1 kGy γ-irradiated Na_2SO_4 nanophosphor

inhibits the radiative recombination of electron and hole centers causing a reduction in TL intensity.

Figure 9a shows the TL glow curves of Na_2SO_4: Dy^{3+} irradiated with γ-rays in the range 0.5–5 kGy. A well-resolved glow peak at ∼170 and ∼61 °C was observed at a heating rate of 5 K s^{-1}. The appearance of two glow peaks in the glow curve indicates that there were possibly two kinds of trapping sites generated due to γ-irradiation. The TL glow peak appearing at ∼170 °C was attributed to host sample, and the other TL glow peak at ∼61 °C was the characteristic of Dy^{3+} ion in Na_2SO_4. The shallow trapping center leads to shouldered peaks at lower temperature and the deeper center gives rise to maximum intensity peak at higher-temperature side.

Figure 10a shows the TL glow curves of $LiNaSO_4$: Dy^{3+} irradiated with γ-rays in the range 0.5–5 kGy. The glow curves of $LiNaSO_4$: Dy^{3+} show the TL signature at ∼100 and ∼180 °C corresponding to high-intensity and

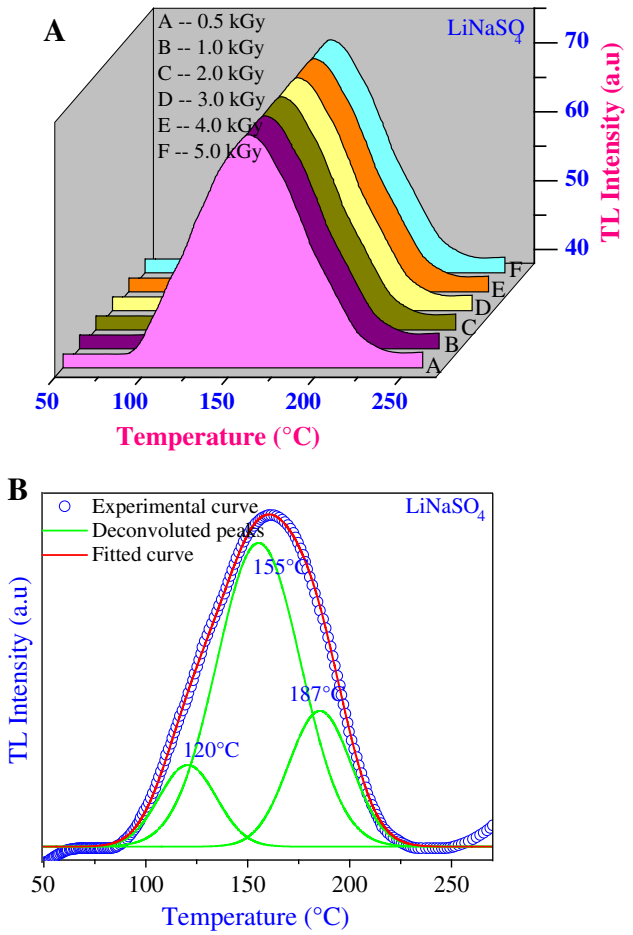

Fig. 8 **a** TL glow curves of γ-irradiated $LiNaSO_4$ nanophosphor (0.5–5 kGy), **b** deconvoluted TL glow curve of 1 kGy γ-irradiated $LiNaSO_4$ nanophosphor

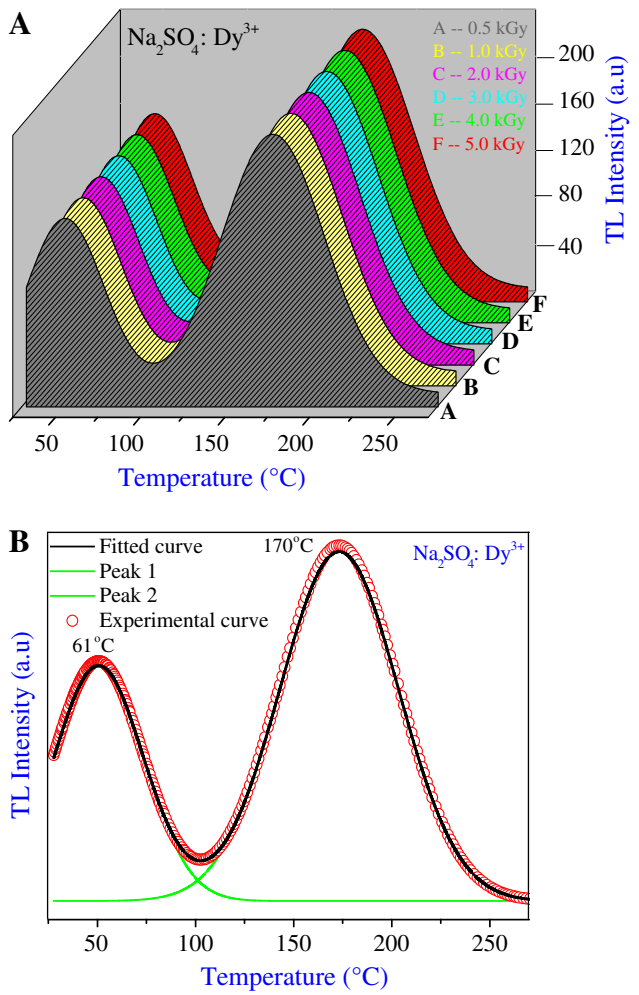

Fig. 9 **a** TL glow curves of γ-irradiated Na_2SO_4: Dy^{3+} nanophosphor (0.5–5 kGy), **b** deconvoluted TL glow curve of 1 kGy γ-irradiated Na_2SO_4: Dy^{3+} nanophosphor

low-intensity peaks, respectively. The appearance of two peaks in the glow curve indicates that there were possibly two kinds of trapping sites generated due to γ-irradiation. Further, it was noticed that there was no appreciable shift in the glow peak positions with increase of gamma dose. In codoping, the shallow trapping center leads to the resolved peak at lower temperature and the deeper center gives rise to shouldered peak at higher temperature. This indicates that in $LiNaSO_4$, Dy^{3+} introduces the mechanism of de-trapping of charges. Most of the charges are released at lower temperature without scattering or residing on the trap states in a comparatively higher TL emission. The deconvoluted glow peaks for Na_2SO_4, $LiNaSO_4$, Na_2SO_4: Dy^{3+} and $LiNaSO_4$: Dy^{3+} are shown in Figs. 7b, 8b, 9b and 10b, respectively.

In radiation dosimetry, efficiency and linearity with dose was highly useful. Therefore, selection of the dopant/synthesis possibly enhances the TL properties, which was further deciding the usage of the material in different fields of dosimetry. In the present investigation, variations in TL glow peak temperature might be attributed to type of irradiation, type of the sample used, amount of irradiation, charge state of the dopant, warming rate, etc. The variations of TL intensity with gamma dose for all the chosen samples are given in Fig. 1s.

The linear/sublinear/supralinear/saturation of TL intensity with dose (gamma) may be explained on the basis of track interaction model [46–48]. This model suggests that the number of created traps as a result of irradiation depends on both the cross-section of the tracks and the length of tracks in the matrix. In nanomaterials, the length of the track may be a few tens of nanometers; as a result, the number of trap centers/luminescence centers will be less for lower doses than their microcrystalline form. However, if we increase the dose, more overlapped tracks occur that may not give extra TL, as a result of which saturation occurs, but in the case of nanomaterials there still exist some particles that would have been missed while

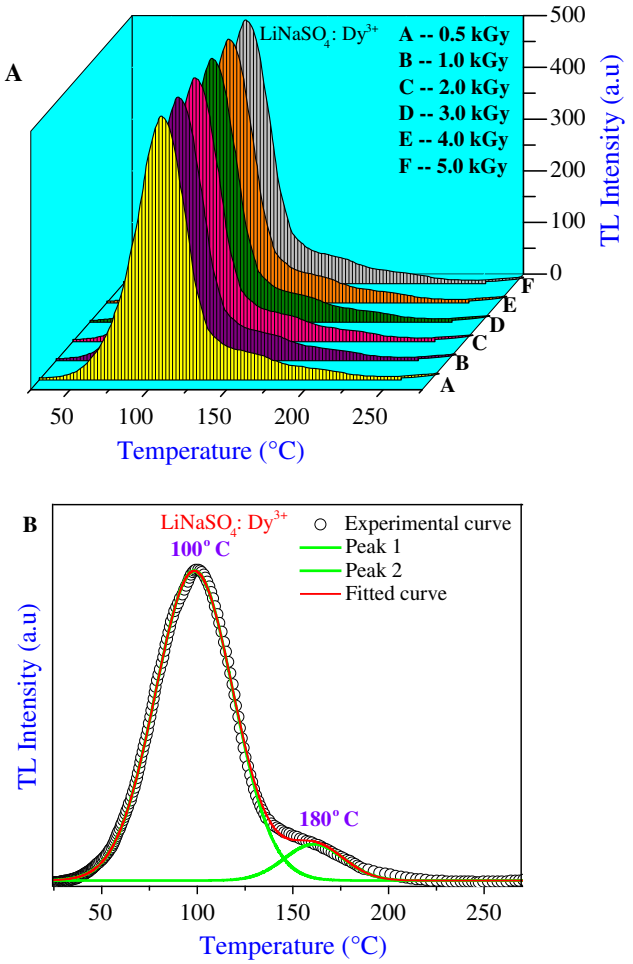

Fig. 10 **a** TL glow curves of γ-irradiated $LiNaSO_4$: Dy^{3+} nanophosphor (0.5–5 kGy), **b** deconvoluted TL glow curve of 1 kGy γ-irradiated $LiNaSO_4$: Dy^{3+} nanophosphor

being targeted by irradiation, due to their tiny size. Thus, on increasing the dose, these nanoparticles, which had earlier been left out from the radiation interaction, now generate trapping and luminescence centers. Thus, we do not get saturation in nanomaterials even at higher doses. However, further higher doses result in saturation or even decrease in TL intensity due to the same reason of overlapping of tracks.

High luminescence yield is a prerequisite for any good TL phosphor. For this purpose, an optimum incorporation of the luminescence centers into the host, local environment around the dopant and doping concentration plays an important role. Figure 2S shows the concentration quenching curve between concentration of Li^+/Dy^{3+} and TL intensity of samples. The TL intensity was found to be maximum for particular concentration (Na_2SO_4: Dy^{3+}—0.06 mol %; $LiNaSO_4$—0.5 mol % and $LiNaSO_4$: Dy^{3+}—0.2 mol %). This may be assigned to the change in trap-state distribution due to lattice perturbation caused by the incorporation of more activator ions in the Na_2SO_4 matrix. The population of recombination and heat generated due to recombination increase with dopant concentration which might shift the TL peak toward higher-temperature side and also increase its intensity. Further increase in dopant concentration, defect sites induced may be inactive or decrease the number of trap sites which may nullify the effect of dopant itself.

3.5.1 TL fading

Fading was an important characteristic feature of dosimetry, which was the unintentional loss of the TL signal. It leads to an under estimation of the absorbed dose. Fading may be due to several causes. Thermal fading originates from the fact that even at RT there was a certain probability of charge carriers escaping from their trapping centers. Fading may also be caused by optical/thermal stimulation. In general, high-sensitivity materials should be handled carefully and stored in opaque containers to prevent fading from light exposure. Other types of fading, which were not temperature dependent, were caused by quantum mechanical tunneling of the trapped charge to recombination sites and transitions between localized states, i.e., transitions that do not take place via the delocalized bands [49]. To study the TL fading effects of the Na_2SO_4, Na_2SO_4: Dy^{3+} (0.06 %), $LiNa_2SO_4$ (0.5 %) and $LiNaSO_4$: Dy^{3+} (0.2 %) nanophosphors were given a test dose of 5 kGy from a γ-source, the TL signal was recorded at different intervals for nearly 30 days. Figure 11 shows the plot of fading ratio (TL Intensity) versus the number of days after γ exposure. Strong fading was observed initially after 5 days, and the

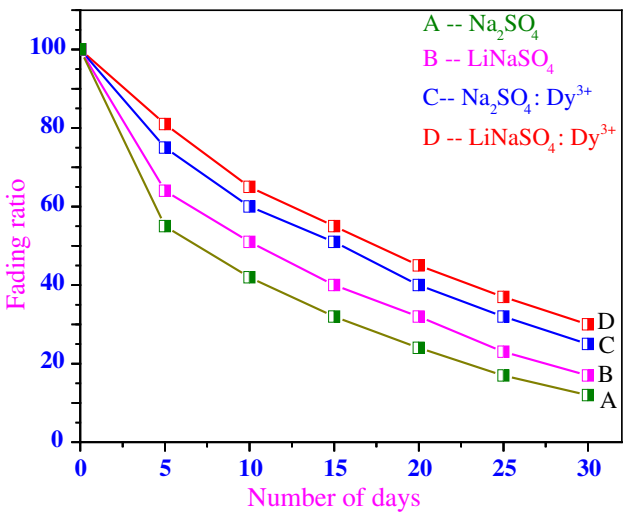

Fig. 11 TL fading of Na_2SO_4, Na_2SO_4: Dy^{3+}, $LiNaSO_4$ and $LiNaSO_4$: Dy^{3+} exposed to 5 kGy of γ-irradiation for a period of 30 days

decay was quite slow and finally stabilizes after 10 days. The extent of fading was found to be less for $LiNaSO_4$: Dy^{3+} compared with Na_2SO_4, Na_2SO_4: Dy^{3+} and $LiNaSO_4$ nanophosphors. Hence, $LiNaSO_4$: Dy^{3+} nanophosphor has potential use in dosimetry.

3.5.2 Calculation of trapping parameters (E, S, b)

TL phosphors generally exhibit glow curves with one or more peaks when the charge carriers were released. The glow curve was characteristic of the different trap levels that lie in the band gap of the material. The traps were characterized by certain physical parameters that include trap depth (E) and frequency factor (s).

For many TL applications, a clear knowledge of these physical parameters was essential [50–52]. To verify further that the activation energies of various TL glow peaks in the γ irradiated samples, the glow curve deconvolutions (GCD) were done (Fig. 3S) using GCD functions, as suggested by Kittis and Gomez-Ros [53], for the first-, second- and general-order kinetics. They were applied to the experimentally obtained glow curves to isolate each peak. Firstly, the highest temperature peak was isolated, and then the order of kinetics as well as the activation energy was calculated using Chen's set of empirical formulae [54].

The activation energy and order of kinetics can be estimated using the following relations:

$$E_\alpha = C_\alpha \left(\frac{kT_m^2}{\alpha}\right) - b_\alpha\,(2kT_m) \tag{6}$$

where $\alpha = \omega,\ \tau,\ \delta$; $\omega = T_2 - T_1$; $\delta = T_2 - T_m$; $\tau = T_m - T_1$

$$C_\tau = 1.51 + 3.0\,(\mu_g - 0.42); \quad b_\tau = 1.58 + 4.2\,(\mu_g - 0.42) \tag{7}$$

$$C_\delta = 0.976 + 7.3\,(\mu_g - 0.42); \quad b_\delta = 0 \tag{8}$$

$$C_\omega = 2.52 + 10.2\,(\mu_g - 0.42); \quad b_\omega = 1 \tag{9}$$

$$\mu_g = \frac{T_2 - T_m}{T_2 - T_1} \tag{10}$$

$$s = \left(\frac{\beta E}{kT_m^2}\right)\left(\frac{\exp\left(E/kT_m\right)}{1 + (b-1)\left(2kT_m/E\right)}\right) \tag{11}$$

where k is the Boltzmann constant $= 8.6 \times 10^{-5}\mathrm{eVK}^{-1}$.

To determine the order of kinetics (b), the form factor μ_g, which involves T_1 and T_2 (temperatures corresponding to half the intensities on either side of the maximum), was calculated. Theoretically, the form factor, which ranges between 0.42 and 0.52, was close to 0.42 for first-order kinetics and 0.52 for second-order kinetics; for other values, it was considered to be general order. Form factor, μ_g, was found to be independent of the activation energy (E) and strongly depends on the order of kinetics. The peak was generated theoretically using these parameters and separated from the main experimental glow curve. Trap depth (E) was calculated using the same set of equations. The procedure was repeated till all the peaks were deconvoluted and the theoretically convoluted curve overlapped the experimentally observed glow curve. The positions of the respective peaks, trapping parameters and order of kinetics for Na_2SO_4, Na_2SO_4: Dy^{3+}, $LiNaSO_4$ and $LiNaSO_4$: Dy^{3+} are shown in Table 5S and Table 6S. The theoretically fitted glow curve is shown in Fig. 3S. After estimation of E, the frequency factor 's' can be obtained using the relation (11). The quality of fit has been tested with the figure of merit (FOM) and was found to be in the range 0.029–0.031 for the theoretical curves were in good agreement and overlap considerably.

4 Conclusions

Na_2SO_4, Na_2SO_4: Dy^{3+}, $LiNaSO_4$ and $LiNaSO_4$: Dy^{3+} samples were successfully synthesized at RT by slow evaporation technique. This method offers wide range of advantages such as voluminous powder (60–70 %), high purity, simple experimental setup and energy saving when compared to other wet chemical methods. The size of the nanoparticles was estimated from the broadenings of the XRD peak which was in good agreement with TEM results. The main interesting feature reported in this work concerns the TL response of Na_2SO_4, $LiNaSO_4$, Na_2SO_4: Dy^{3+} and $LiNaSO_4$: Dy^{3+} over a very wide range (0.5–5 kGy). TIM model was used here to explain the linear behavior with γ-dose. Finally, it can be concluded that a easy method of preparation, good sensitivity, simple glow curve structure, linear response over a wide range of γ-exposure and low fading are some of the good characteristics of the prepared nanophosphors. Among all the prepared nanophosphors, $LiNaSO_4$: Dy^{3+} shows the better characteristics, making it useful for dosimetric applications.

Acknowledgments One of the authors, Y. S. Vidya is thankful to 'ISRO-ISEC, advanced devices and radiation cell, Bangalore,' for providing γ-irradiation facility. The author also wishes to thank Dr. S. C. Prashantha, H. O. D, Department of Physics, EWIT, Bangalore, and Department of Physics, Lal Bahadur Shastri Government First Grade College, R. T. Nagar, Bangalore, for their support.

References

1. C.F. Wu, W.P. Qin, G.S. Qin, D. Zhao, J.S. Zhang, S.H. Huang, S.Z. Lv, H.Q. Liu, H.Y. Lin, Appl. Phys. Lett. **82**, 520 (2003)
2. J. Dexpert Ghys, R. Mauricot, M.D. Faucher, J. Lumin. **69**, 203 (1996)

3. B. Bihari, H. Eilers, B.M. Tissue, J. Lumin. **75**, 1 (1997)
4. B. Li, Z.N. Gu, J.H. Lin, M.C. Su, Chem. J. Chin. Univ. **22**, 1 (2001)
5. Z.H. Jia, H. Li, Z.R. Ye, Chem. J. Chin. Univ. **23**, 352 (2002)
6. S.P. Lochab, P.D. Sahare, R.S. Chauhan, N. Salah, A. Pandey, J. Phys. D Appl. Phys. **39**, 1786 (2006)
7. E. Wiedemann, G.C. Schmidt, Ann. Phys. Chem. **54**, 600 (1895)
8. T. Yamashita, N. Nada, H. Onishi, S. Kitamura, in *Proceedings of the 2nd International Conference on Luminescence Dosimetry*, Gatlinberg, USA, 1968
9. T. Yamashita, N. Nada, H. Onishi, S. Kitamura, Health Phys. **21**, 295 (1971)
10. Yamashita T, in *Proceedings of the 4th International Conference on Luminescence Dosimetry*, Krakow, Poland, 1974, p. 467
11. J.P. Elder, Thermochim. Acta **36**, 67 (1980)
12. H.G. Wiedemann, Thermochim. Acta **50**, 17 (1981)
13. S. Gomathy, P. Gopalan, A.R. Kulakarni, J. Sol. Stat. Chem. **146**, 6 (1999)
14. F.C. Kracek, R.E. Gibson, J. Phys. Chem. **34**, 188 (1930)
15. B.K. Choi, H.K. Lee, Y.W. Kee, Sol. Stat. Ionics **113–115**, 493 (1998)
16. C.R. Navarro, E. Doehne, E. Sebastian, Cem. Concr. Res. **30**, 1527 (2000)
17. P.D. Sahare, S.V. Moharil, Radiat. Eff. Def. Solids **114**, 167 (1990)
18. P.D. Sahare, S.V. Moharil, Radiat. Eff. Def. Solids. **116**, 275 (1991)
19. P.D. Sahare, S.V. Moharil, J. Lumin. **43**, 369 (1989)
20. P.D. Sahare, S.V. Moharil, B.D. Bhasin, J. Phys. D Appl. Phys. **22**, 971 (1989)
21. A.Z.M.S. Rahman, X. Cao, L. Wei, B. Wang, R. Yu, Z. Chen, G. An, A. Sidike, Appl. Phys. A **111**, 587 (2013)
22. A. Sidike, A.Z.M.S. Rahman, J.Y. He, K. Atobe, N. Yamashita, J. Lumin. **129**, 1271 (2009)
23. A. Sidike, A.Z.M.S. Rahman, J.Y. He, L.X. Gong, K. Atobe, N. Yamashita, J. Lumin. **131**, 1840 (2011)
24. V. Correcher, J.G. Guinea, P.L. Arce, J.M.G. Ros, Spectrochim. Acta A. **60**(7), 1431 (2004)
25. A. Pandey, P.D. Sahare, Phys. Status Solids (a) **199**, 533 (2003)
26. A. Pandey, P.D. Sahare, J.S. Bakare, S.P. Lochab, F. Singh, D. Kanjilal, J. Phys. D **36**, 633 (2003)
27. R. Murugan, A. Ghule, H. Chang, J. Phys. Condens. Matter. **12**, 677 (2000)
28. P. Parhi, V. Munivannan, Mater. Lett. **62**, 3468 (2008)
29. M. Morgano, I.P. Wurfl, S. Binetti, Sci. Adv. Mater. **3**, 388 (2011)
30. Y.R. Jung, H.K. Yang, B.K. Moon, B.C. Choi, J.H. Jeong, H. Choi, J.H. Kim, K.H. Kim, J. Nanosci. Nanotechnol. **11**, 871 (2011)
31. C. Manjunatha, D.V. Sunitha, H. Nagabhushana, B.M. Nagabhushana, S.C. Sharma, R.P.S. Chakradhar, Spectrochim. Acta Part A **93**, 140 (2012)
32. A. Periasamy, S. Murugananda, M. Palaniswamy, J. Chem. **2**, 981 (2009)
33. B.K. Choi, D.J. Lockwood, J. Phys. Condens. Matter. **17**, 6095 (2005)
34. C.R. Navarro, E. Doehne, E. Sebastian, Cem. Concr. Res. **30**, 1527 (2000)
35. P. Klug, L.E. Alexander, *X-ray Diffraction Procedure* (Wiley, New York, 1954)
36. S.B. Qadri, J.P. Yang, E.F. Skelton, B.R. Ratan, Appl. Phys. Lett. **70**, 1020 (1997)
37. P. Parhi, V. Munivannan, Mater. Lett. **62**, 3468 (2008)
38. A. Periasamy, S. Murugananda, M. Palaniswamy, J. Chem. **2**, 981 (2009)
39. L.K. Pan, Q. Sun Chang, C.M. Li, J. Phys. Chem. B **108**, 3404 (2004)
40. H.Q. Cao, X.Q. Qiu, B. Luo, Y. Liang, Y.H. Zhang, R.Q. Tan, M.J. Zhao, Q.M. Zhu, Adv. Funct. Mater. **14**, 243 (2004)
41. A. Emeline, G.V. Kataeva, A.S. Litke, A.V. Rudakova, V.K. Ryabchuk, N. Serpone, Langmuir **14**, 5011 (1998)
42. J. Tauc, in *Optical Properties of Solids*, ed. by F. Abeles (North Holland, Amsterdam, 1970)
43. N. Dhananjaya, H. Nagabhushana, B.M. Nagabhushana, B. Rudraswamy, D.V. Sunitha, C. Shivakumara, R.P.S. Chakradhar, J. Spectrochim. Acta A. **96**, 532 (2012)
44. C. Furetta, *Handbook of Thermoluminescence* (World Scientific, Singapore, 2003)
45. S.P. Lochab, P.D. Sahare, R.S. Chauhan, N. Salah, A. Pandey, J. Phys. D Appl. Phys. **39**, 589 (2009)
46. R. Chen, S.W.S. Mckeever, *Theory of Thermoluminescence and Related Phenomenon* (World Scientific Press, Singapore, 1997)
47. S.P. Lochab, P.D. Sahare, R.S. Chauhan, N. Salah, A. Pandey, J. Phys. D Appl. Phys. **39**, 1786 (2006)
48. Y.S. Horowitz, M. Rosenkrantz, S. Mahajna, D. Yossian, J. Phys. D Appl. Phys. **29**, 205 (1996)
49. Y.S. Horowitz, O. Avila, M. Rodrigues-Villafurete, Nucl. Instrum. Methods B **184**, 85 (2001)
50. A.J.J. Boss, Nucl. Instrum. Methods B **184**, 3 (2001)
51. G. Kitis, C. Furetta, M. Prokic, V. Prokic, J. Phys. D Appl. Phys. **33**, 1252 (2000)
52. B. Arunakumar Sharma, A. Nabachandra Singh, S. Nabadwip Singh, O. Binoy Kumar Singh, Rad. Meas. **44**, 32 (2009)
53. G. Kitis, J. M. Gomez-Ros, Nucl. Instrum. Methods A **440**, 224 (2000)
54. R. Chen, Y. Kirish, *Analysis of Thermally Stimulated Processes* (Pergamon, NewYork, 1981)